Journal of Catalysis 272 (2010) 262–274

Contents lists available at ScienceDirect

Journal of Catalysis

journal homepage: www.elsevier.com/locate/jcat

N_2O decomposition over Fe-zeolites: Structure of the active sites and the origin of the distinct reactivity of Fe-ferrierite, Fe-ZSM-5, and Fe-beta. A combined periodic DFT and multispectral study

Stepan Sklenak [a,*], Prokopis C. Andrikopoulos [a], Bundet Boekfa [a], Bavornpon Jansang [a], Jana Nováková [a], Lubomir Benco [b], Tomas Bucko [b], Juergen Hafner [b], Jiří Dědeček [a], Zdeněk Sobalík [a]

[a] J. Heyrovský Institute of Physical Chemistry of the Academy of Sciences of the Czech Republic, Dolejškova 3, 182 23 Prague 8, Czech Republic
[b] Institut für Materialphysik and Center for Computational Materials Science, Universität Wien, Sensengasse 8, A-1090 Vienna, Austria

ARTICLE INFO

Article history:
Received 30 October 2009
Revised 31 March 2010
Accepted 10 April 2010
Available online 15 May 2010

Keywords:
N_2O decomposition
Fe in ferrierite
Fe in ZSM-5
Fe in the beta zeolite
DFT
VASP

ABSTRACT

The N_2O decomposition over Fe-ferrierite, Fe-beta, and Fe-ZSM-5 has been recently studied [K. Jisa, J. Novakova, M. Schwarze, A. Vondrova, S. Sklenak, Z. Sobalik, J. Catal. 262 (2009) 27] and a superior activity of Fe-ferrierite with respect to Fe-beta and Fe-ZSM-5 has been shown. In this study, we investigated (1) plausible active sites for the N_2O decomposition over Fe-ferrierite and (2) the origin of the distinct reactivity of Fe-ferrierite, Fe-ZSM-5 and Fe-beta employing a combined theoretical (periodic DFT) and experimental (UV–vis–NIR spectroscopy, IR spectroscopy, ^{29}Si MAS NMR spectroscopy and catalytic batch experiments) approach. We evidenced that two Fe(II) cations accommodated in two adjacent six-membered rings in the eight-membered ring channel (β sites) of Fe-ferrierite (the calculated Fe–Fe distance is 7.4 Å) form the active site responsible for the superior activity of this catalyst in the N_2O decomposition in the absence of NO. Similar structures can be formed in Fe-beta. However, the probability of their formation is very low. For Fe-ZSM-5, the geometrical arrangement of the cationic positions is far from that in Fe-ferrierite and it is not suitable for the N_2O decomposition. Therefore, the predicted order of the activity of the Fe(II) exchanged zeolites agrees with our experimental findings and it is: Fe-ferrierite $\gg$ Fe-beta > Fe-ZSM-5. We further showed that the accommodation of divalent cations in rings forming cationic sites can lead to significant rearrangements of the local structures of the zeolite framework, and therefore, the precise structure of sites binding a divalent cation cannot be derived from results of X-ray diffraction experiments, but can be inferred from theoretical calculations.

1. Introduction

In the past 10 years, attention was drawn to development of methods for the abatement of N_2O. Transition metal-exchanged silicon-rich zeolites are excellent candidates for the decomposition of nitrous oxide to nitrogen and oxygen. Fe-ZSM-5 was studied the most both experimentally [1–8] and theoretically [9–15] but Fe-ferrierite [16,17] as well as Fe-beta [17–20] were also investigated. Our recent study [21] showed that Fe-zeolite samples prepared by Fe(III) precipitation using organic solvent represent promising catalytic systems with a high and stable activity under conditions of nitrous acid plants. The catalytic activity of Fe-ferrierite in the absence of NO was found to be superior with respect to Fe-beta and Fe-ZSM-5 (ferrierite $\gg$ the beta zeolite > ZSM-5). On the other hand, all the three zeolites have similar activities in the presence of NO [21]. We suggested that a collaboration of two Fe(II) cations accommodated in two adjacent sites located on the opposite sides of the eight-membered ring channel can explain the superior performance of Fe-ferrierite [21].

In this article, we focus on the investigation and detailed description of (1) plausible active sites of Fe-ferrierite and their structures, (2) the origin of the distinct reactivity of Fe-ferrierite, Fe-ZSM-5, and Fe-beta, (3) the very first steps of the N_2O decomposition, i.e. the adsorption of N_2O on Fe(II) located in the active sites and the subsequent release of molecular nitrogen to form FeO(ad). We will explore the differences between the isolated and two cooperating adjacent cationic sites. The course of the entire N_2O decomposition on Fe-ferrierite to form N_2 and O_2 is very complex (e.g. [8,10,12,13,22–26]) as it involves many reaction steps. It is a subject of our next study.

2. Experimental

NaK-ferrierite (Tosoh, Japan; Si/Al 8.6), NH_4-beta zeolite (Zeolyst; Si/Al 15.5), and Na-ZSM-5 (VURUP, SR; Si/Al 13.4) were used

* Corresponding author.
E-mail address: stepan.sklenak@jh-inst.cas.cz (S. Sklenak).

0021-9517/$ - see front matter © 2010 Elsevier Inc. All rights reserved.
doi:10.1016/j.jcat.2010.04.008

as parent zeolites to prepare the catalysts. The parent samples of ferrierite and ZSM-5 were converted to a NH_4^+ form by three times repeated equilibration with 1 M NH_4NO_3. Fe was introduced in the zeolite samples employing an impregnation of the parent ammonia zeolite forms by anhydrous $FeCl_3$ in acetylacetone. The method for introduction of Fe is described in detail elsewhere [27]. The resulting Fe/Al ratios were 0.12, 0.13, and 0.11 for ferrierite, the beta zeolite, and ZSM-5, respectively. The samples of the three zeolites were the same as those used in our recent study [21].

^{29}Si MAS NMR experiment was carried out on the hydrated NaK-ferrierite sample utilizing a Bruker Avance 500 MHz (11.7 T) Wide Bore spectrometer using 4 mm o.d. ZrO_2 rotor with a rotation speed of 5 kHz. A ^{29}Si MAS NMR high-power decoupling experiment with a $\pi/6$ (1.7 μs) excitation pulse, a relaxation delay of 30 s, and a 50% ramp cross polarization (CP) pulse sequence was applied to collect a single pulse and cross polarization spectra. The ^{29}Si chemical shifts were referenced to Q8M8.

UV–vis–NIR spectra of the hydrated Fe-zeolite samples in the range from 200 to 2200 nm were collected using a Perkin–Elmer Lambda 950 spectrometer equipped with Spectralon™ integration sphere. Spectralon™ served also as the reference. WinLab software was applied to recalculate spectra using the Schuster–Kubelka–Munk equation [28].

IR spectra with a resolution of 2 cm^{-1} of the Fe-ferrierite sample were measured at ambient temperature after evacuation (10^{-3} Pa) of the sample at 450 °C in a standard glass vacuum cell equipped with KBr windows using a FTIR spectrometer Nexus 670 (ThermoNicolet). The samples were used as self-supported pellets with the thickness from 5 to 10 mg/cm^2. The spectra intensities were normalized on the sample with the thickness of 5.5 mg/cm^2 using the integral area of the zeolite skeletal bands in the region between 1750 and 2100 cm^{-1}. The positions and relative intensities of the bands in the "skeletal transmission window" (the region between 950 and 880 cm^{-1}, where the antisymmetric T–O–T stretching lattice vibrations were observed) were evaluated by a Fourier self-deconvolution procedure (OMNIC 4.1 software) and spectral fitting procedure using Origin 7.5 software assuming Gaussian profiles, respectively, of the spectra. For details of this method, see Refs. [28–30].

Batch catalytic experiments were carried out in a reaction vessel (175 cm^3) at 230 and 280 °C. The samples were pretreated in situ in vacuum at 450 °C for 2 h and then cooled to the reaction temperatures. Then nitrous oxide (500 Pa) reacted with the pretreated sample for 40 min. Following that the reaction mixture was analyzed in a Balzers QMG 420 quadrupole mass spectrometer calibrated using individual reaction components.

3. Experimental results

3.1. ^{29}Si NMR spectroscopy

^{29}Si MAS NMR spectrum of the parent ferrierite sample and its analysis is shown in Fig. 1. The spectrum is similar to those already reported for a ferrierite sample [31]. Six resonances at −115.3, −110.8, −108.6, −105.0, −102.1 and, −98.9 ppm are present in the spectrum. A cross-polarization experiment reveals (not shown in the figure) that the resonance at −98.9 ppm corresponds to terminal silanol groups (SiOH). The resonances at −108.6, −105.0 and −102.1 ppm are assigned to Si(3Si,1Al) atoms, while the resonances at −115.3 and −110.8 ppm reflect Si(4Si) atoms. A detailed analysis of ^{29}Si MAS NMR spectra of zeolites is described elsewhere [32–34]. The assignment of the resonances to the individual types of Si atoms was confirmed by quantitative analysis of the framework Al content in zeolite. The Si/Al_{FR} value of 8.5 was calculated using equation

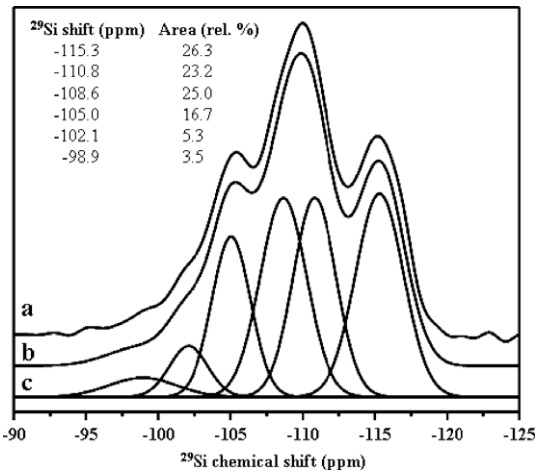

Fig. 1. ^{29}Si MAS NMR spectrum of NaK-ferrierite. Experimental spectrum (a), spectrum simulation (b) and individual Gaussian bands of the spectrum simulation (c).

$$Si/Al_{FR} = I/\Sigma 0.25 \cdot n \cdot I_n$$

where I denotes the total intensity of the ^{29}Si NMR signal in the single pulse experiment and I_n denotes the intensities of the NMR signals corresponding to the Si(4−nSi, nAl) atoms [34]. Si/Al_{FR} is in good agreement with the results of chemical analysis (8.6). Other interpretations of the spectra resulted in unrealistic values of Si/Al_{FR}. Thus, it can be concluded that Si(2Si, 2Al) atoms, i.e. Al–O–Si–O–Al sequences, are not present in the investigated ferrierite sample.

3.2. UV–vis–NIR spectroscopy

Normalized UV–vis–NIR spectra of the hydrated Fe-zeolite samples with low Fe/Al values (<0.15) (after impregnation, thermal treatment and rehydration on air) are shown in Fig. 2. Four types of bands can be resolved in the spectrum. The UV bands around 36,000 and 44,000 cm^{-1} correspond to Fe(III)O or Fe(II) charge transfer bands. These bands are unspecific and can correspond to solvated isolated Fe ions or Fe ion oligomeric species or Fe ions in oxides. The band around 29,000 cm^{-1} can be attributed to the charge transfer of Fe(III)O in binuclear Fe(III) species [28,35]. The UV bands between 29,000 and 44,000 cm^{-1} are present in the spectra of all three samples. The bands between 16,000 and 26,000 cm^{-1} (easily distinguishable in the spectrum of the Fe-beta zeolite) can be assigned to pair transitions and charge transfer of

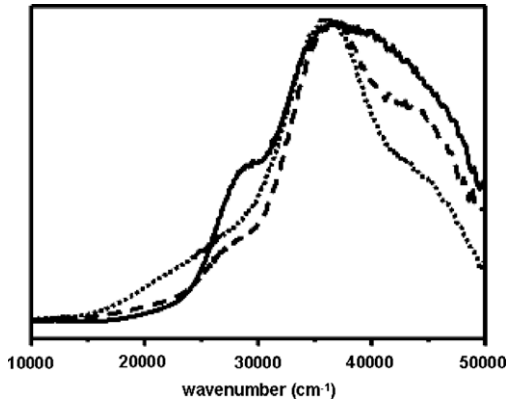

Fig. 2. Normalized UV–vis–NIR spectrum of as prepared Fe-ferrierite (—), Fe-ZSM-5 (— —) and Fe-beta (■■■).

Fe(III) oxide species. Also the weak band at 12,000 cm^{-1} is unspecific and can correspond to the d–d transitions of both isolated Fe(III) ions and Fe(III) ions in oxide [28,36].

Binuclear Fe(III) species observed in fully hydrated samples evidenced by the band around 29,000 cm^{-1} are significantly present in Fe-ferrierite, while their concentration in Fe-ZSM-5 is significantly lower and difficult to estimate in Fe-beta due to an overlap with the bands of Fe pair transitions (from 16,000 to 26,000 cm^{-1}) and the strong UV band at 36,000 cm^{-1}. On the other hand, the presence of Fe(III) oxides in Fe-beta is significant, while only traces of Fe(III) oxides can be detected in Fe-ZSM-5 and there are no iron oxides in Fe-ferrierite.

3.3. IR spectroscopy

FTIR spectrum of the dehydrated Fe-ferrierite sample (Fig. 3) features a broad band ascribed to shifted antisymmetric T–O–T stretching lattice modes induced by binding bare Fe(II) ions to the framework oxygens [37]. Deconvolution of the spectrum with the subtracted background (Fig. 3) yielded two individual bands at 940 and 915 cm^{-1} corresponding to two different local perturbations of the framework induced by the accommodation of Fe(II) in the α and β cationic sites, respectively [37]. Quantitative analysis of the FTIR spectrum under the assumption that the extinction coefficients of the individual bands are the same [37] indicates that Fe(II) ions located in the β site predominate (85% of Fe(II) ions in the zeolite) in the Fe-ferrierite sample.

3.4. Catalytic experiments

Batch catalytic experiments allow investigating the very first steps of the N_2O decomposition on Fe-ferrierite, Fe-beta, and ZSM-5, i.e. the adsorption of N_2O on Fe(II) located in the active sites and the following release of molecular nitrogen to form FeO(ad).

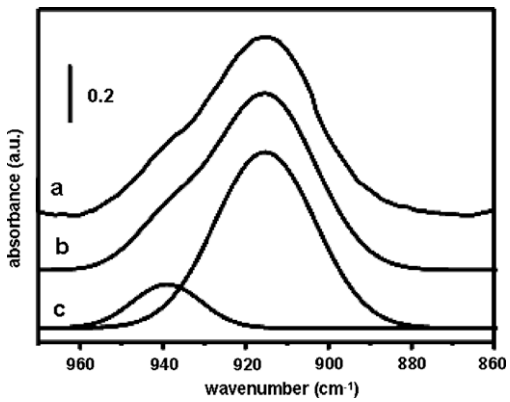

Fig. 3. FTIR spectrum of Fe-ferrierite featuring shifted antisymmetric T–O–T stretching lattice vibrations (a), spectra simulation (b), and Gaussian bands corresponding to the Fe(II) in α (940 cm^{-1}) and β (915 cm^{-1}) sites (c).

Table 1
Amounts[a] of decomposed N_2O and released O_2 in μmol/g after 40 min at 230 and 280 °C.

Zeolite	230 °C		280 °C	
	N_2O	O_2	N_2O	O_2
Fe-ferrierite	5.9	0.3	26	6.8
Fe-beta	1.9	0	4.6	0.6
Fe-ZSM-5	2	0	2.9	0.3

[a] The starting amount of N_2O is 32 μmol/g. The total decomposition of N_2O would result in 16 μmol/g of released O_2 if there is no capture of oxygen on the active zeolite centers.

The results of the batch experiments at 230 and 280 °C are shown in Table 1. The N_2O decomposition over Fe-ferrierite at 230 °C as well as Fe-beta and Fe-ZSM-5 at 280 °C yields only negligible amounts of O_2. Therefore, we can assume that the decomposition involves almost exclusively the adsorption of N_2O on Fe(II) to give FeO(ad) and N_2(g). The subsequent reaction steps which would produce O_2(g) can be neglected. Our test at 230 °C clearly evidences a superior activity of Fe-ferrierite over the other two zeolites, while the results obtained at 280 °C reveal a significantly higher activity of Fe-beta over Fe-ZSM-5.

4. Accommodation of divalent cations in pentasil zeolites

4.1. Cationic sites

Fe(II) cations as well as other divalent metal cations can occupy in pentasil zeolites (e.g. mordenite, ferrierite, ZSM-5, and the beta zeolite) three types of cationic sites designated as α, β, and γ [38–41]. These three cationic sites for divalent cations were determined using XRD for mordenite [42,43] and suggested employing UV–vis spectroscopy of bare Co(II) ions as a probe for ZSM-5 [38], the beta zeolite [41], and ferrierite [40] for which the sites were later confirmed by synchrotron powered XRD [44–46]. The three cationic sites exhibit significant similarities but they differ in their detailed geometrical arrangement.

The α cationic site represents an elongated six-membered ring which is composed of two five-membered rings. The accommodated cation exhibits an open coordination sphere, since it is located at the top of a pyramid with the base formed by four oxygen atoms of the six-membered ring. This site is easily accessible because it is present on the wall of the main channel in ferrierite, and on the wall of the sinusoidal channel of ZSM-5. But for the beta zeolite, this site exhibits a low accessibility, since it faces the inner space of a cage of the beta zeolite.

The β cationic site in ferrierite, ZSM-5, and the beta zeolite corresponds to a deformed six-membered ring. The cation is located near the plane of the six-membered ring, and therefore, the accommodated cation exhibits an open coordination sphere. The β cationic site can be easily reached because it is positioned in (1) an eight-membered ring channel of ferrierite, (2) channel crossing in ZSM-5, (3) the wall of a cage of the beta zeolite.

The boat-shaped γ cationic site is a complex location formed by four five-membered rings (ferrierie) or two five-membered and two six-membered rings (ZSM-5). For the beta zeolite, this site is located inside a beta cage. Accommodated cations are assumed to exhibit a closed coordination sphere with a pseudo-octahedral coordination. Therefore, only the α and β cationic sites will be considered in this study.

The structures of cationic sites accommodating divalent cations in different zeolite frameworks were subject of several studies [47–49]. They indicated that the cations prefer to bind to oxygen atoms of AlO_4 tetrahedra. We will employ molecular dynamics (MD) simulations to investigate the structure and stability of the α, $\beta-1$, and $\beta-2$ sites accommodating Fe(II).

4.2. Al distribution in the rings forming cationic sites

Two Al atoms located in the α cationic site are required to accommodate a divalent cation. The location of a divalent bare cation in the vicinity of only one framework Al with a distant second framework Al is of very low probability because of the high reactivity of such a cation [50]. Our ^{29}Si MAS NMR experiments (see Section 3.1.) revealed that Al–O–Si–O–Al sequences are not present in the ferrierite sample used. Therefore, there is only one possible arrangement of two Al atoms in the α site (Fig. 4). On the contrary,

there are two possible distributions of two Al atoms forming the $\beta-1$ and $\beta-2$ sites (Fig. 4).

4.3. Cooperation of two adjacent sites accommodating Fe(II) cations

Besides the cationic site accessibility and the local structure, the distance between two cations accommodated in individual positions of the zeolite frameworks plays a significant role if two active sites are involved in the catalyzed reaction. Rough estimates of the distances between cations accommodated in two distinct sites were estimated using models of the zeolite structures based on the X-ray diffraction data [51,52].

Two α cationic sites in ferrierite are located at the opposite sides of the ferrierite main channel and they face each other. The distance between the two cations in these sites is about 6.0 Å (Fig. S1 of the Supplementary material). Two β sites in ferrierite are present in the eight-membered ring channels and also face each other. The distance between two cations in these two sites is calculated to be 7.4 Å (Figs. 5 and 6).

Two α sites of ZSM-5 are located on the opposite sides of the main channel but they do not face each other because they are shifted in the opposite directions along the channel axes. Thus, the distance between two cations in these sites is about 7.0 Å (Fig. S2 of the Supplementary material). Two β sites of ZSM-5 at the channel crossing face each other and the distance of two cations in these sites is about 4.5 Å (Fig. S3. of the Supplementary material).

The distance between two cations accommodated in two β sites of the beta zeolite is about 8.0 Å (Fig. S4. of the Supplementary material). The β sites face each other and they are located across the channel of the beta zeolite. The distances between two cations located in two α sites of the beta zeolite are not taken into account because these sites are not accessible.

It should be noted that the above discussed distances reflect only the structures of the zeolite framework and do not include the probability of the presence of two Al atoms in the six-membered ring forming the cationic site. Our prior study [40] of the same ferrierite sample revealed that there was a high probability of a formation of two adjacent β cationic sites each with two Al atoms in the ferrierite sample, for details see Section 8.2. Moreover, binuclear Fe(III)···Fe(III) species are present in the hydrated oxidized Fe-ferrierite sample, as evidenced by the presence of the band around 29,000 cm^{-1} in the Fe-ferrierite sample (see Section 3.2.). Thus, both single Fe(II) cations located in isolated sites

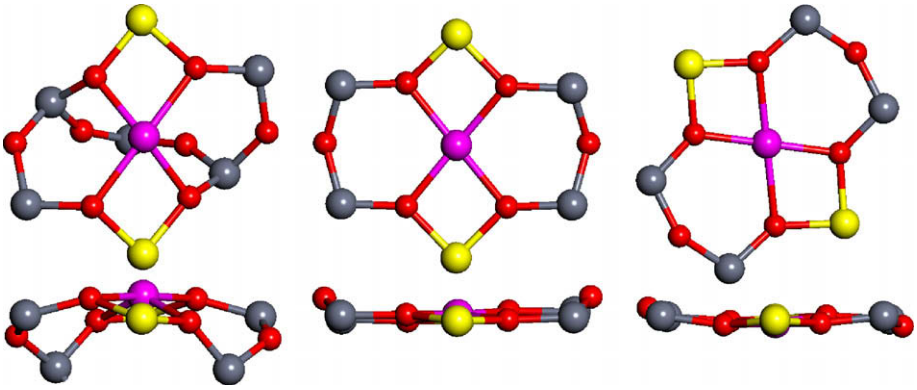

Fig. 4. Possible arrangements of two Al atoms in the six-membered rings forming the α site (left), $\beta-1$ (middle), and $\beta-2$ (right) sites. Silicon atoms are in gray, aluminum atoms in yellow, iron atoms in violet, and oxygen atoms in red. (For interpretation of the references to colour in this figure legend, the reader is referred to the web version of this article.)

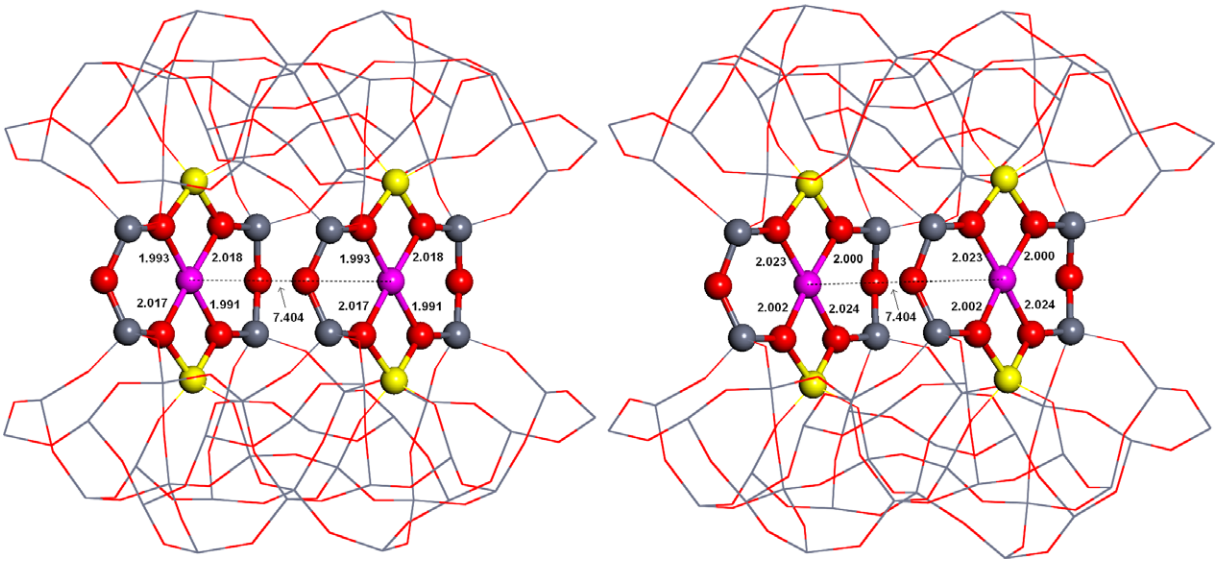

Fig. 5. Optimized structures of the $\beta-1$ site ($\beta-1+\beta-1$ model) before (left) and after (right) molecular dynamics simulations. The distances are in Å. Silicon atoms are in gray, aluminum atoms in yellow, iron atoms in violet, and oxygen atoms in red. (For interpretation of the references to colour in this figure legend, the reader is referred to the web version of this article.)

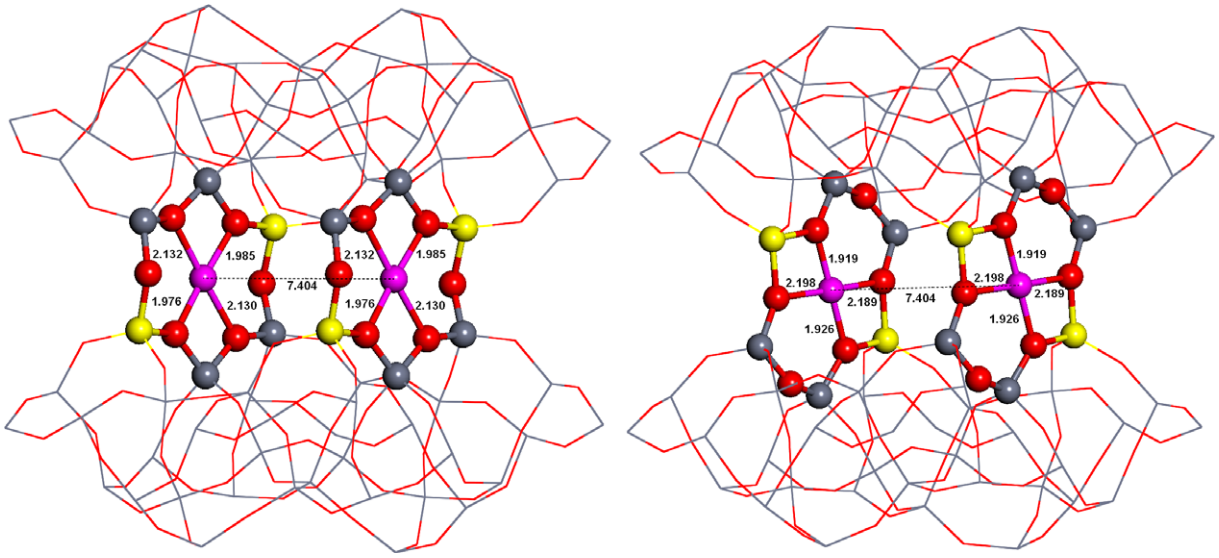

Fig. 6. Optimized structures of the $\beta-2$ site ($\beta-2+\beta-2$ model) before (left) and after (right) molecular dynamics simulations. The distances are in Å. Silicon atoms are in gray, aluminum atoms in yellow, iron atoms in violet, and oxygen atoms in red. (For interpretation of the references to colour in this figure legend, the reader is referred to the web version of this article.)

as well as two close Fe(II) cations located in two adjacent β sites are assumed to exist in the Fe-ferrierite catalyst [21] with low or medium Fe loadings. Therefore, the properties of both former and latter Fe(II) cations are studied employing computational methods.

5. Computational details

5.1. Structural models

The starting structures were generated from the experimental orthorhombic structure of ferrierite determined by neutron diffraction [53]. Five models possessing the P1 symmetry were employed to investigate five distinct possible arrangements of the active sites in ferrierite. The first three models (α, $\beta-1$, and $\beta-2$; see Figs. 7–9, respectively) represent isolated cationic sites which do not allow interactions of the O atom of the adsorbed N_2O with another Fe(II) located in a close cationic position, while the other two models ($\beta-1+\beta-1$ and $\beta-2+\beta-2$; see Figs. 5 and 6, respectively) feature two cooperating adjacent Fe(II) cationic sites permitting interactions of N_2O with both Fe(II) cations. Sites accommodating Fe(II) in the beta zeolite and ZSM-5 are not modeled. Our results obtained for the α, $\beta-1$, and $\beta-2$ models of ferrierite will serve as estimates of the outcome of calculations of isolated cationic sites of the beta zeolite and ZSM-5.

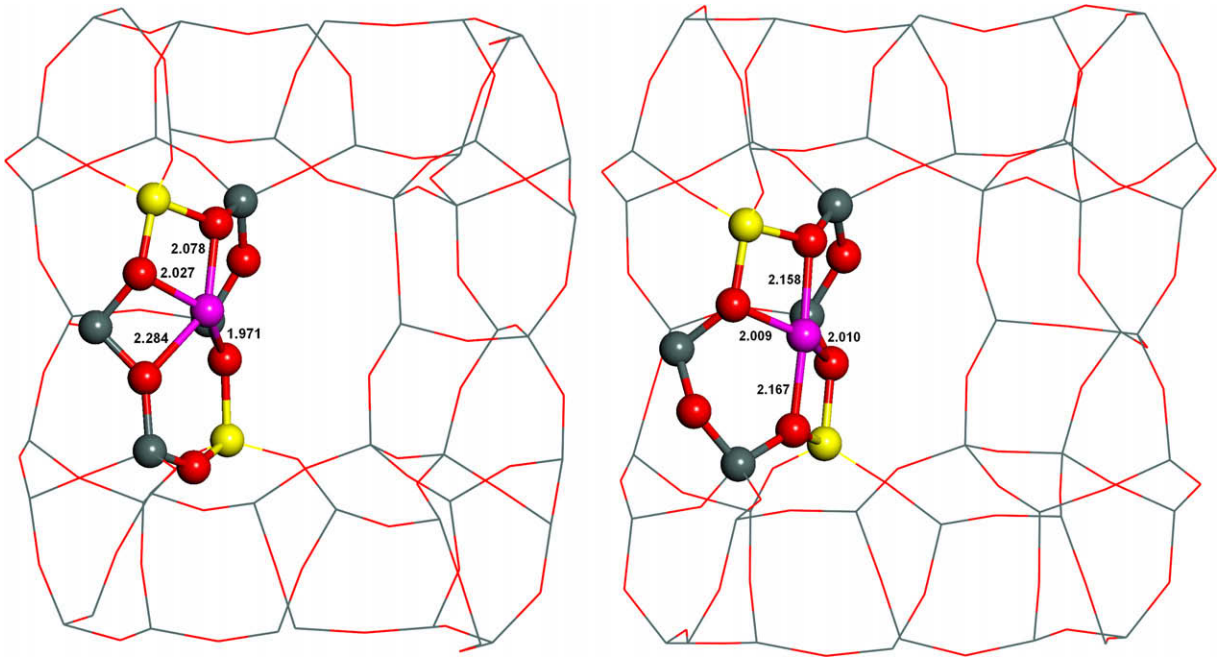

Fig. 7. Optimized structures of the α site (α model) before (left) and after (right) molecular dynamics simulations. The distances are in Å. Silicon atoms are in gray, aluminum atoms in yellow, iron atoms in violet, and oxygen atoms in red. (For interpretation of the references to colour in this figure legend, the reader is referred to the web version of this article.)

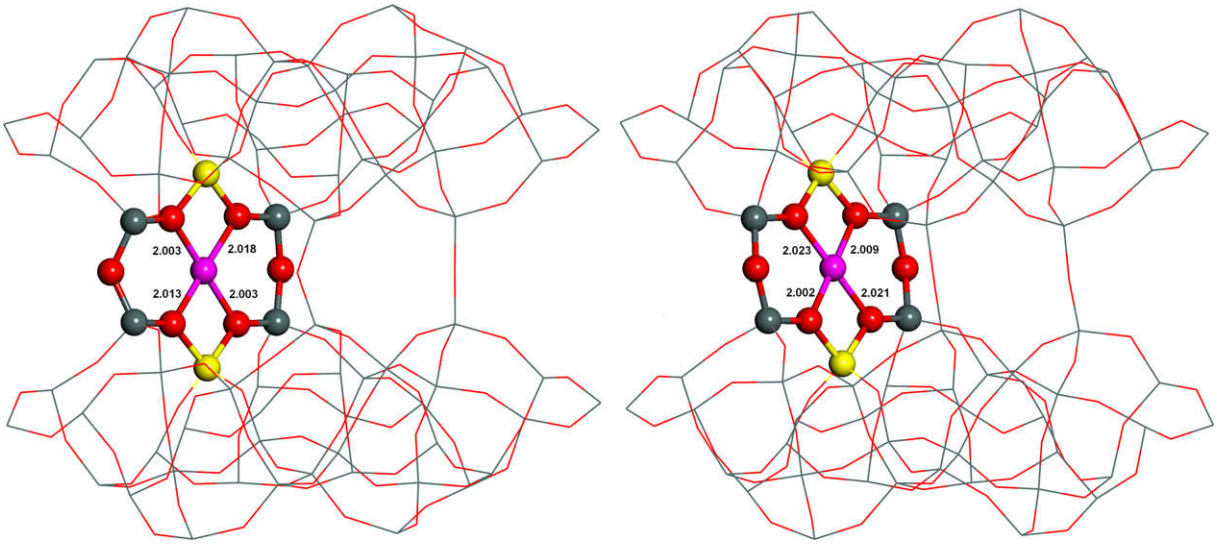

Fig. 8. Optimized structures of the $\beta-1$ site ($\beta-1$ model) before (left) and after (right) molecular dynamics simulations. The distances are in Å. Silicon atoms are in gray, aluminum atoms in yellow, iron atoms in violet, and oxygen atoms in red. (For interpretation of the references to colour in this figure legend, the reader is referred to the web version of this article.)

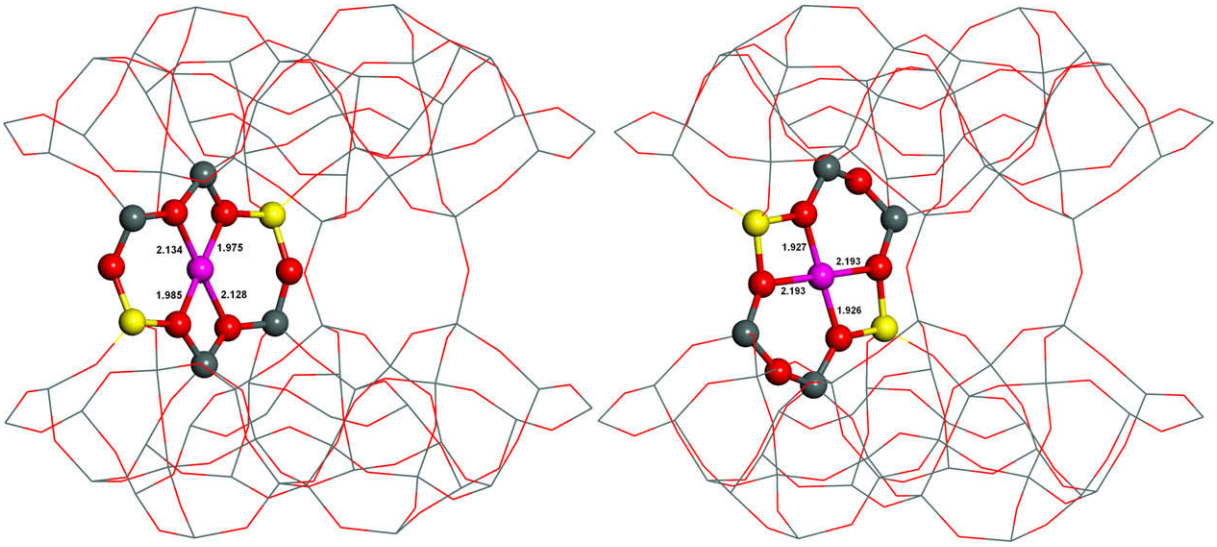

Fig. 9. Optimized structures of the $\beta-2$ site ($\beta-2$ model) before (left) and after (right) molecular dynamics simulations. The distances are in Å. Silicon atoms are in gray, aluminum atoms in yellow, iron atoms in violet, and oxygen atoms in red. (For interpretation of the references to colour in this figure legend, the reader is referred to the web version of this article.)

The α model utilizes one unit cell of ferrierite (a = 18.651, b = 14.173, and c = 7.404 Å) with two Al/Si substitutions in the α site (Fig. 7) accommodating one Fe(II) cation. The $\beta-1$, $\beta-2$, $\beta-1+\beta-1$, and $\beta-2+\beta-2$ models (Figs. 8, 9, 5 and 6, respectively) employ a super cell composed of two unit cells along the c dimension. The $\beta-1$ and $\beta-2$ models feature one $\beta-1$ and $\beta-2$ site, respectively, (2 Al and 1 Fe(II) per super cell) and the other unit cell is all-silica, while the $\beta-1+\beta-1$ and $\beta-2+\beta-2$ models have two $\beta-1$ and $\beta-2$ sites (one per unit cell), respectively, (4 Al and 2 Fe(II) per super cell).

5.2. Electronic structure calculations

Spin polarized periodic DFT calculations were carried out employing the VASP code [54–57]. Bonding of the Fe(II) cation to a zeolite matrix conserves the high-spin configuration Fe $d^5\uparrow$ $d^1\downarrow$ with a magnetic moment of 4 μ_B suggested by Hund's rule for the free Fe(II) cation [50,58]. The Kohn–Sham equations were solved variationally in a plane-wave basis set using the projector-augmented wave (PAW) method of Blöchl [59], as adapted by Kresse and Joubert [60]. The exchange–correlation energy was described by the PW91 generalized gradient approximation (GGA) functional [61,62]. Brillouin zone sampling was restricted to the Γ-point. The plane-wave cutoff of 400 eV was utilized for geometry optimizations, while a smaller cutoff of 300 eV was used for the molecular dynamics simulations.

5.3. Geometry optimizations

The atomic positions were optimized at constant volume employing a conjugate-gradient algorithm minimization of energies and forces while the lattice parameters were fixed at their

experimental values. Transition structures were identified using the dimer method [63], as recently improved by Heyden et al. [64].

5.4. Molecular dynamics

The molecular dynamics (MD) simulations used the exact Hellmann–Feynman forces acting on atoms and applied the statistics of the canonical ensemble to the motion of the atomic nuclei [65] using the Verlet velocity algorithm [66,67] to integrate Newton's equations of motion. The time step for the integration of the equations of motion was 1 fs. The simulations were run for 5 ps at 300 K for each of the five investigated models. The structures of ten distinct "snapshots" collected from the last 500 fs of each molecular dynamics simulation were optimized. The most stable conformer for each of the five investigated models was then used for subsequent calculations.

6. Computational results

6.1. Structure and stability of the Fe(II) cationic sites

Our MD calculations of the five models revealed the stability of the α, β − 1, and β − 2 cationic sites. The optimized structures before and after molecular dynamics calculations are shown in Figs. 5–9. The structure of the β − 1 cationic site in the β − 1 as well as β − 1 + β − 1 models (Figs. 8 and 5, respectively) is only slightly changed, while the geometry of the α and β − 2 cationic sites differ significantly after the MD simulations of the α, β − 2, and β − 2 + β − 2 models (Figs. 7, 9 and 6). The calculated Fe–O bond lengths range from 2.01 to 2.17 Å for the α site, from 2.00 to 2.02 Å for the β − 1 site, and from 1.92 to 2.20 Å for the β − 2 site.

Table 2
Stabilization energy[a] in kcal/mol of the cationic sites accommodating Fe(II) for the five models.

Model	ΔE	ΔE[b]
α	−11.0	−11.0
β − 1	−4.5	−4.5
β − 1 + β − 1	−3.8	−1.9
β − 2	−12.0	−12.0
β − 2 + β − 2	−22.3	−11.2

[a] The difference between the energies of the model relaxed by MD simulations and subsequently optimized and the model which was not relaxed by MD simulations but simply optimized using the starting structure determined by neutron diffraction [53].
[b] Stabilization energy per cationic site.

Surprisingly, the calculated Fe–Fe distance of the active site is 7.404 Å for both β − 1 + β − 1 and β − 2 + β − 2 models before as well as after MDs (Figs. 5 and 6).

Our MD simulations of the five models and subsequent optimizations of the selected MD snapshots led to energy stabilizations relative to the five models which were not relaxed employing MD simulations but simply optimized using the structure determined by neutron diffraction [53] as the starting geometry. The stabilization is significant for the β − 2 and α sites, while it is moderate for the β − 1 site. The corresponding values for the five models are listed in Table 2. The largest stabilization is obtained for the β − 2 site (−22.3 and −12.0 kcal/mol for the β − 2 + β − 2 and β − 2 models, respectively) which also rearranges its structure the most. The α site is similarly stabilized (−11.0 kcal/mol for the α model) as β − 2, while the energy of the β − 1 site drops only slightly (−3.8 and −4.5 for the β − 1 + β − 1 and β − 1 models, respectively).

6.2. N_2O adsorption and N–O cleavage on isolated Fe(II) cations

The optimized structures of all the calculated species are shown in Figs. 10 and 11, S5, and S6 of the Supplementary material). Scheme 1 reveals the adsorption energies of N_2O on Fe(II) accommodated in isolated cationic sites. N_2O coordinates preferably by the N terminal atom (Fig. 10). The strongest interaction is with Fe(II) in the α cationic site (α model): −12.3 and −9.0 kcal/mol for N terminal and O atom adsorption, respectively. The interaction with Fe(II) in the β − 2 site (β − 2 model) is weaker (−10.9 and −5.7 kcal/mol for the N terminal and O atom adsorption, respectively). Fe(II) located in the β − 1 site (β − 1 model) interacts only weakly with the N terminal atom of N_2O (−8.4 kcal/mol) and the Fe···ONN complex is not formed at all. Scheme 1 further shows that after N_2O is adsorbed by the O atom (α and β − 2), the O–N bond is cleaved to form FeO(ad) and N_2(g) (Figs. S5 and S6). The corresponding barriers and reaction energies are 17.6/19.1 (α/β − 2) and −7.7/−10.5 (α/β − 2) kcal/mol, respectively.

6.3. N_2O adsorption and N–O cleavage on two cooperating Fe(II) cations

Figs. 12 and 13, S7, and S8 of the Supplementary material depict the optimized structures of the calculated species. The energies and barriers of the adsorption of N_2O on Fe(II) accommodated in two adjacent collaborating β sites and the following reaction steps leading to FeO(ad) and N_2(g) are shown in Scheme 2. N_2O interacts preferably by the N terminal atom (Fig. 12). The adsorption of N_2O is stronger on Fe(II) located in the β − 2 site (β − 2 + β − 2 model):

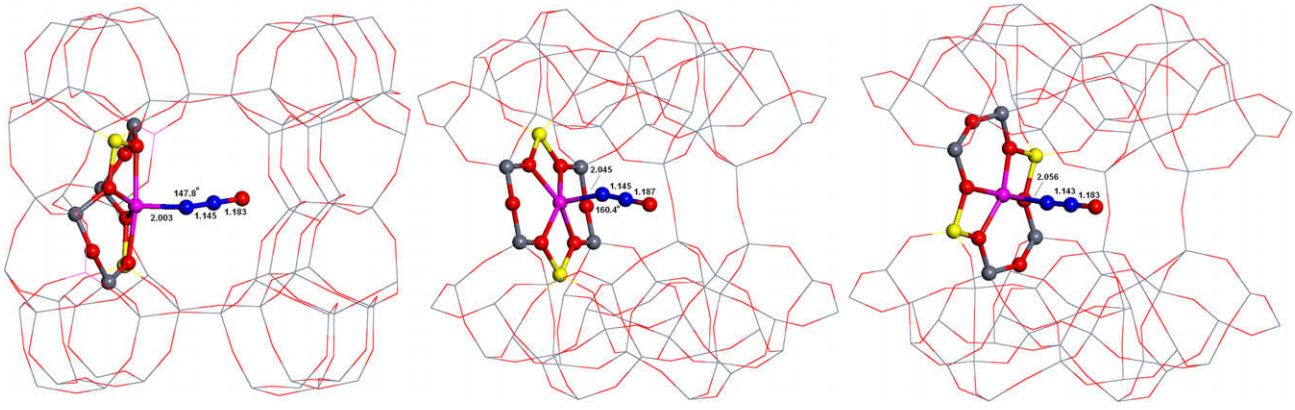

Fig. 10. Optimized structures of the Fe···NNO complex formed in the α site (α model) (left), β − 1 site (β − 1 model) (middle), and β − 2 site (β − 2 model) (right). The distances are in Å. Silicon atoms are in gray, aluminum atoms in yellow, iron atoms in violet, nitrogen atoms in blue, and oxygen atoms in red. (For interpretation of the references to colour in this figure legend, the reader is referred to the web version of this article.)

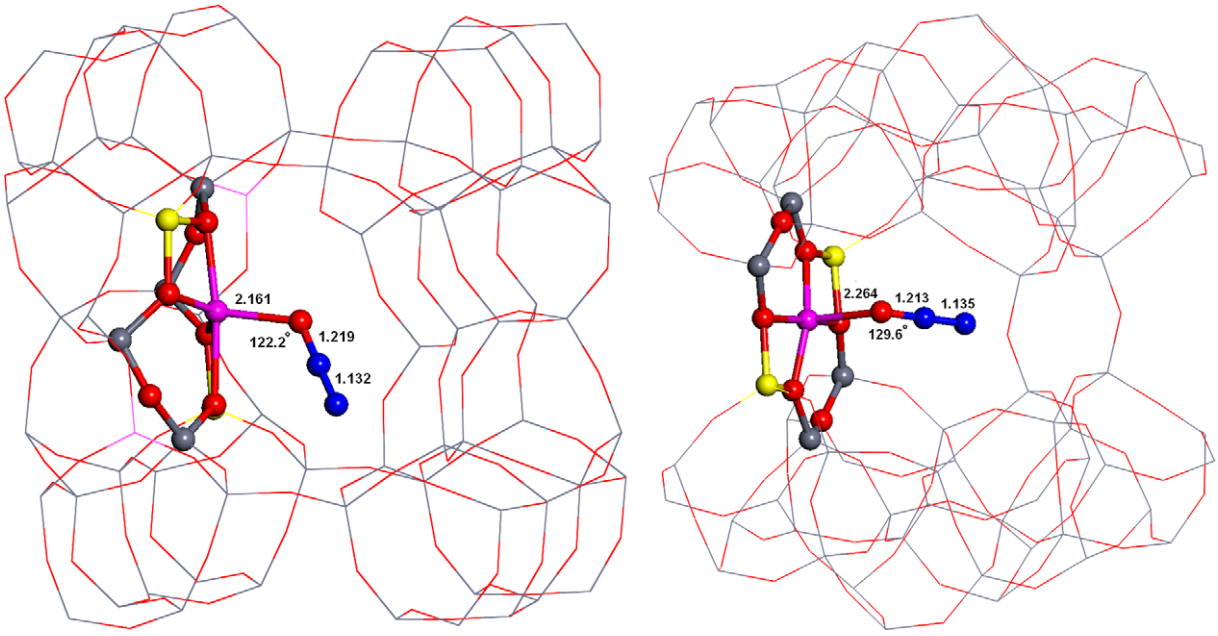

Fig. 11. Optimized structures of the Fe···ONN complex formed in the α site (α model) (left) and $\beta-2$ site ($\beta-2$ model) (right). The distances are in Å. Silicon atoms are in gray, aluminum atoms in yellow, iron atoms in violet, nitrogen atoms in blue, and oxygen atoms in red. (For interpretation of the references to colour in this figure legend, the reader is referred to the web version of this article.)

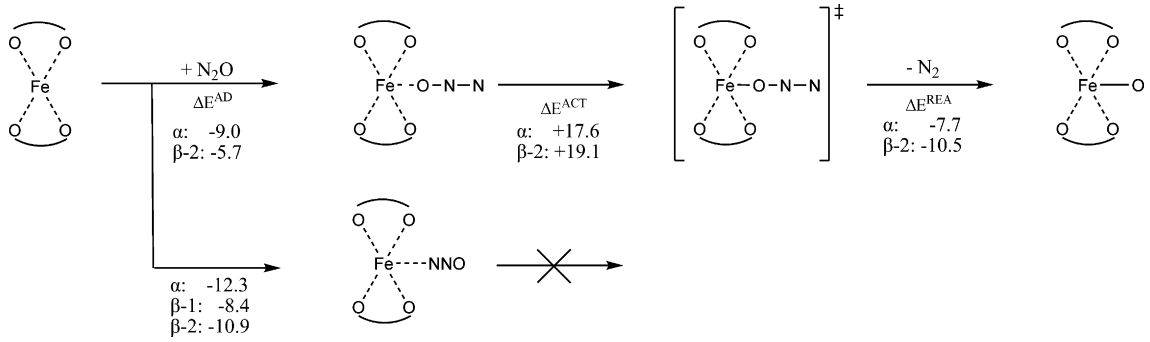

Scheme 1. Energies and barriers of the adsorption of N_2O on Fe(II) accommodated in isolated α and β sites and the following reaction steps leading to FeO(ad) and N_2(g).

−9.5 (N terminal atom) and −3.7 (O atom) kcal/mol than on Fe(II) accommodated in the $\beta-1$ site ($\beta-1+\beta-1$ model): −5.0 kcal/mol (N terminal atom) and no interaction between the O atom of N_2O and Fe(II) is observed. Subsequently, the N–O bond is cleaved to yield FeO(ad) and N_2(ad) (Figs. 13 and S8). The corresponding barrier is 9.4 and 12.3 kcal/mol for the $\beta-1+\beta-1$ and $\beta-2+\beta-2$ models, respectively. The reaction energies of the N–O bond cleavage to yield FeO(ad) and N_2(ad) are −15.2/−17.8 ($\beta-1+\beta-1/\beta-2+\beta-2$). The adsorption of N_2(ad) on Fe(II) is weak (−2.3 ($\beta-1+\beta-1$) and −7.4 ($\beta-2+\beta-2$) kcal/mol).

7. Rearrangement of cationic sites accommodating Fe(II) cations

The structure of sites binding divalent cations were estimated using X-ray diffraction experiments only for mordenite [42,43,68,69] and ferrierite frameworks [44–46,70,71]. However, the obtained structures of the cationic positions represent a superposition of different arrangements of these sites with and without accommodated divalent cations. Moreover, some rings forming vacant cationic sites contain two Al atoms which are needed for the site to ligate a divalent cation, while other rings include only one or no Al atom (then the rings are not able to accommodate a divalent cation). These issues result in a significant decrease in the accuracy of the X-ray diffraction determined structure of the framework oxygen atoms involved in coordinating the divalent cation. However, the structure of sites accommodating a divalent cation can be inferred from theoretical calculations.

The starting structures used in this study were generated from the experimental orthorhombic structure of ferrierite determined by neutron diffraction [53]. Divalent metal cations located in sites prefer to coordinate to oxygen atoms of AlO_4^- tetrahedra rather than SiO_4 tetrahedra, since the cations compensate the negative charge of AlO_4^-. However, the starting structures featured this proper coordination of Fe(II) to four oxygen atoms of two AlO_4^- tetrahedra only for the $\beta-1$ site (Figs. 8 and 5), while the Fe(II) cation is ligated to only three and two oxygen atoms of two AlO_4^- tetrahedra for the α (Fig. 7) and $\beta-2$ (Figs. 9 and 6) sites, respectively. The other one (α site) and two ($\beta-2$) oxygen atoms belong to SiO_4 tetrahedra. Therefore, the structure of the α and $\beta-2$ sites coordinating Fe(II) (α, $\beta-2$, and $\beta-2+\beta-2$ models) significantly rearranged during the MD calculations. The Fe(II) cation correctly coordinates to four oxygen atoms of two AlO_4^- tetrahedra in the

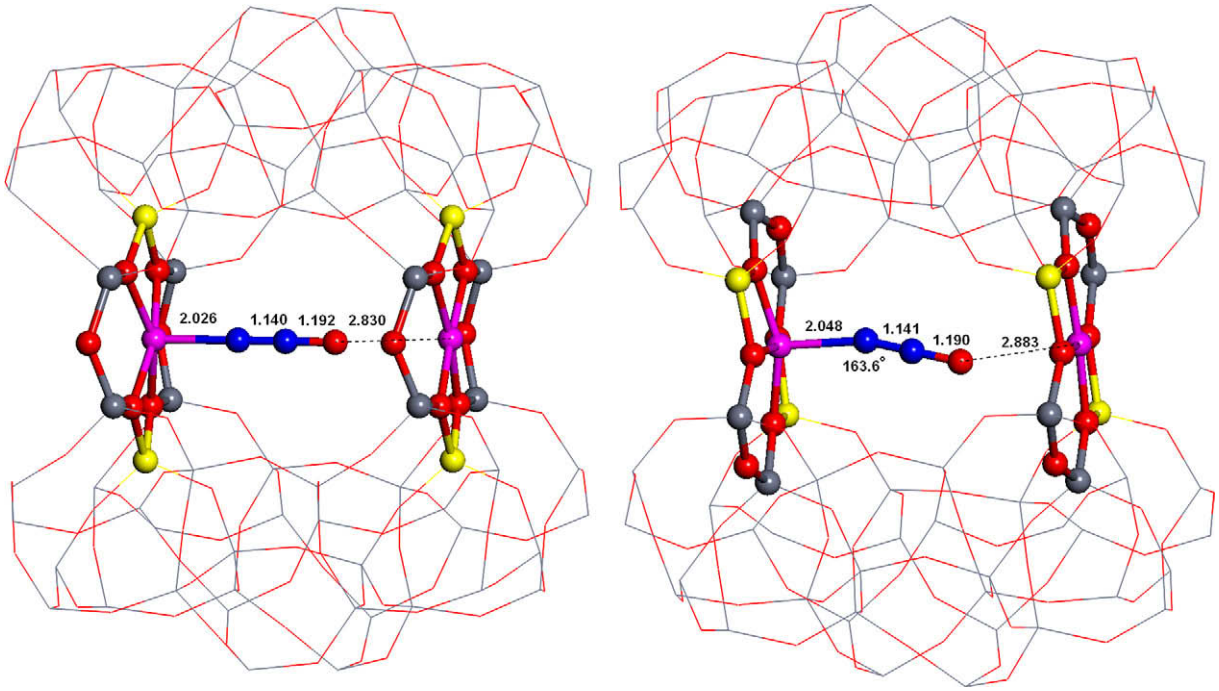

Fig. 12. Optimized structures of the [Fe···NNO Fe] complex formed in the $\beta-1$ site ($\beta-1+\beta-1$ model) (left) and $\beta-2$ site ($\beta-2+\beta-2$ model) (right). The distances are in Å. Silicon atoms are in gray, aluminum atoms in yellow, iron atoms in violet, nitrogen atoms in blue, and oxygen atoms in red. (For interpretation of the references to colour in this figure legend, the reader is referred to the web version of this article.)

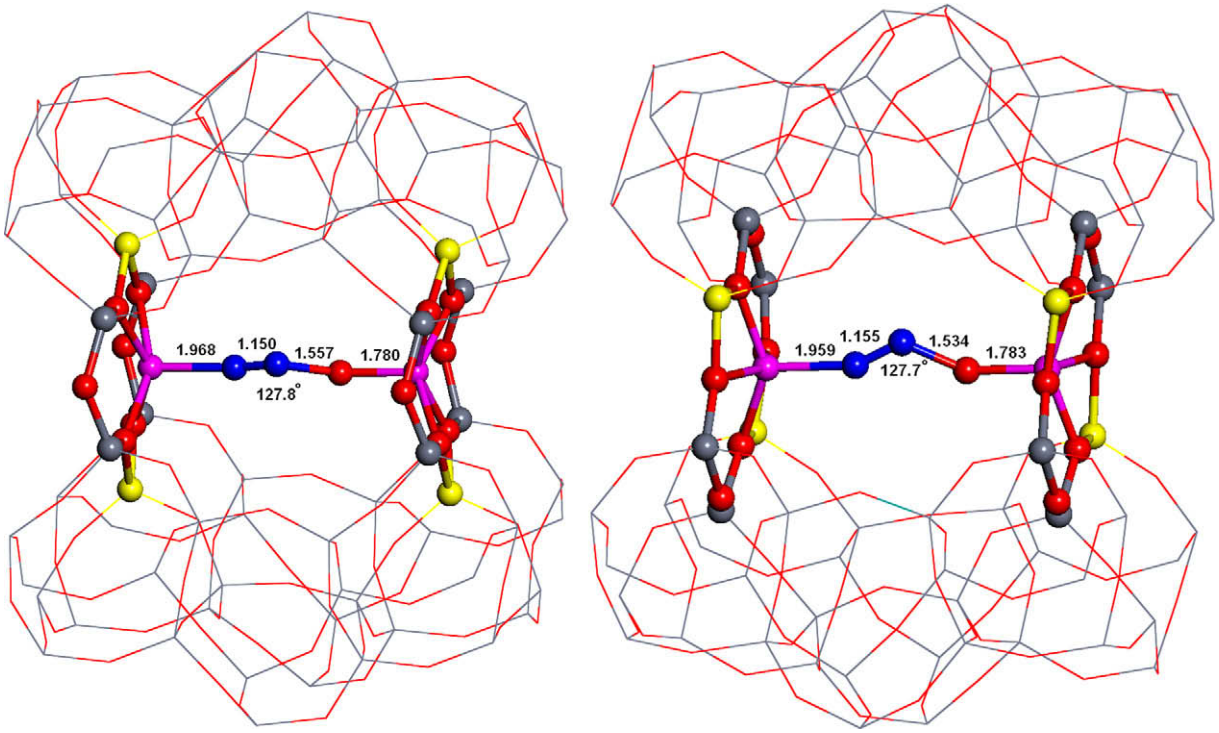

Fig. 13. Optimized structures of the transition state (N–O cleavage) formed in the $\beta-1$ site ($\beta-1+\beta-1$ model) (left) and $\beta-2$ site ($\beta-2+\beta-2$ model) (right). The distances are in Å. Silicon atoms are in gray, aluminum atoms in yellow, iron atoms in violet, nitrogen atoms in blue, and oxygen atoms in red. (For interpretation of the references to colour in this figure legend, the reader is referred to the web version of this article.)

resulting structures (Figs. 7, 9 and 6) of the α, $\beta-2$, and $\beta-2+\beta-2$ models. On the other hand, the structure of the $\beta-1$ site in the $\beta-1$ and $\beta-1+\beta-1$ models (Figs. 8 and 5) did not noticeably rearrange since the coordination of Fe(II) was correct in the starting structures, only the frameworks slightly relaxed. The similarity of the structures of the $\beta-1$ and $\beta-2$ cationic sites accommodating Fe(II) is in good agreement with the observation that only one type of the β site accommodating bare Co(II) cations was determined by Vis spectroscopy of dehydrated Co-ferrierite [29,40,72]. The Co(II) coordination is almost identical

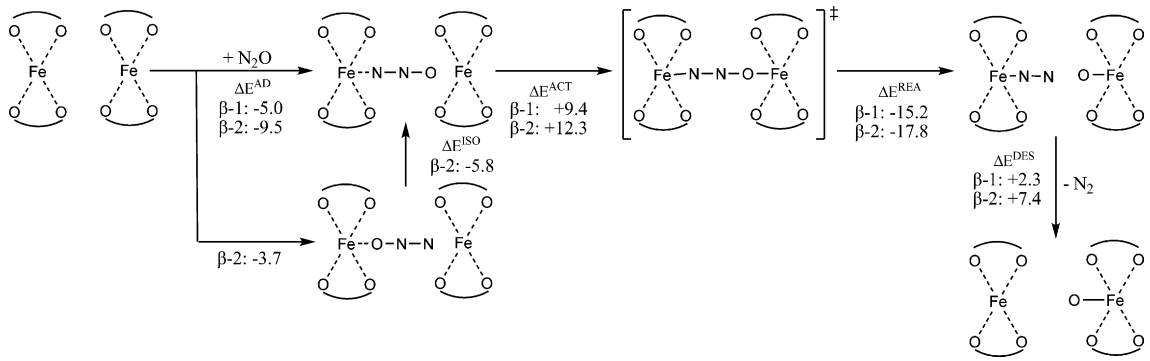

Scheme 2. Energies and barriers of the adsorption of N_2O on Fe(II) accommodated in two adjacent collaborating β sites and the following reaction steps leading to FeO(ad) and N_2(g).

in both $\beta-1$ and $\beta-2$ sites, and therefore, they cannot be distinguished by Vis spectroscopy of Co(II) ions as a probe.

The stabilization of the α and $\beta-2$ sites due to the rearrangement is calculated to be about −11 to −12 kcal/mol per site while the relaxation of the framework for the $\beta-1$ and $\beta-1+\beta-1$ models leads to a small drop of the energy by about 4 kcal/mol regardless of whether the model includes one or two $\beta-1$ sites (Table 2).

8. Discussion

8.1. The effect of the cooperation of two Fe(II) sites on the N_2O adsorption and N–O cleavage

Schemes 1 and 2 show the very first steps of the N_2O decomposition, i.e. the adsorption of N_2O on Fe(II) accommodated in the active sites and the subsequent release of molecular nitrogen to form FeO(ad). N_2O can adsorb on Fe(II) by both the terminal atoms; however, the adsorption by the terminal N atom is significantly stronger. Therefore, almost all N_2O molecules coordinate to Fe(II) by the terminal N to give the Fe···NNO complex. Further reactions steps differ depending on whether Fe(II) is accommodated in an isolated site or two cooperating adjacent sites.

Fe(II) present in an isolated site (Scheme 1) is blocked, since it forms the Fe···NNO complex and the N_2O decomposition cannot proceed. Only a tiny fraction of N_2O molecules ligate to Fe(II) located in isolated α and $\beta-2$ sites by the O atom to form the Fe···ONN complex while there is no such adsorption for Fe(II) in an isolated $\beta-1$ site. The N–O bond of the Fe···ONN complex can cleave to yield FeO(ad) and N_2(g). The calculated barrier is 17.6 and 19.1 kcal/mol for the isolated α and $\beta-2$ sites, respectively. However, since the Fe···ONN complex is less stable than the Fe···NNO complex, the barrier of the N–O cleavage calculated from the more stable complex (Fe···NNO) is higher by the difference between the adsorption energies of the Fe···NNO and Fe···ONN complexes and thus reaching 20.9 and 24.3 kcal/mol for isolated α and $\beta-2$ sites, respectively.

The course of the very first steps of the N_2O decomposition notably differs when N_2O can interact with two Fe(II) cations accommodated in two adjacent β sites (Scheme 2). N_2O adsorbs to one of the Fe(II) cations by the terminal N atom to form the [Fe···NNO Fe] complex. The O atom of the adsorbed N_2O in [Fe···NNO Fe] is well positioned for the N–O cleavage, since its distance to the other Fe(II) cation is about 3 Å and all five atoms (Fe, N, N, O, and Fe) lie approximately in a line. This unique arrangement causes the N–O cleavage facile. The calculated barriers are only 9.4 and 12.3 kcal/mol for the $\beta-1$ and $\beta-2$ sites, respectively. A tiny fraction of N_2O molecules coordinate with Fe(II) located in two adjacent $\beta-2$ sites by the O atom to form the [Fe···ONN Fe] complex, while there is no such adsorption in two adjacent $\beta-1$ sites. [Fe···ONN Fe] very easily isomerizes into [Fe···NNO Fe].

Our calculations reveal that the presence of the second Fe(II) cation coordinated in an adjacent β site has a dramatic effect on the course of the very first steps of the N_2O decomposition. The adsorption of N_2O by the N terminal atom blocks the active site composed of an isolated Fe(II) cationic site. Then the N–O cleavage can proceed only when N_2O adsorbs by the O atom. This adsorption is energetically strongly disfavored. The consequence is that the N–O cleavage is sluggish for isolated α and $\beta-2$ sites (barriers reaching 20.9 and 24.3 kcal/mol, respectively) and does not occur for the isolated $\beta-1$ site. On the other hand, when two Fe(II) cations accommodated in two adjacent β sites can collaborate then the N–O cleavage is facile (barriers are only 9.4 and 12.3 kcal/mol for the $\beta-1$ and $\beta-2$ sites, respectively).

The N_2O decomposition to form FeO(ad) and N_2(g) is calculated to be exothermic for all three cationic sites for both isolated sites as well as two adjacent collaborating β sites, see Schemes 1 and 2.

The structure of the transition state involving two Fe cations [Fe(1)···NNO–Fe(2)] (Fig. 13) reveals the geometrical requirements for the active site. The distance between the O atom of N_2O and Fe(2) is about 1.8 Å, the N–O bond is elongated to around 1.6 Å, the N–N bond length is about 1.2 Å, and the Fe(1)···N distance is about 2.0 Å. The N and O atoms of the NNO moiety pull the Fe cations out of the plane of the ring forming the β cationic sites by ca 0.2 Å for the complexes (Fig. 12) and more than 0.6 Å for the transition state (Fig. 13). The Fe–Fe distance decreases from 7.4 Å in Fe-ferrierite (Figs. 5 and 6) to 7.2 Å in the complexes (Fig. 12) and further to 6.2 Å in the transition state (Fig. 13). Since the Fe(II) cations are pulled out from the plane of the ring at least by 0.2 Å, we assume that the value of 6.6 Å (6.2 + 0.2 + 0.2) is the minimum distance between two Fe(II) in Fe-zeolite needed for the transition state to occur. On the other hand, we can estimate the maximum distance between two collaborating Fe(II) assuming that the transition state has a linear arrangement, and furthermore, the bond distances are close to those in the transition state (Fig. 13). Only the Fe(1)···N distance might be larger up to about 2.2 Å. In addition, the cations can be pulled out of the plane of the ring by up to 0.7 Å. Therefore, we estimate that maximum span between the two cooperating Fe(II) is 8.2 Å (1.8 + 1.6 + 1.2 + 2.2 + 0.7 + 0.7).

Our theoretical results suggesting that two adjacent collaborating β sites represent the active center for the N_2O decomposition over the low Fe loaded ferrierite are in good agreement with experimental findings that cooperating Fe(II)···Fe(II) species represent beside isolated Fe(II) ions a significant fraction of the Fe(II) species in the investigated ferrierite sample. The formation of Fe oxide was not observed in the investigated sample.

Binuclear Fe(III)-oxo complexes are evidenced by UV–vis–NIR spectroscopy (band around 29,000 cm^{-1}) (Fig. 2) in as prepared hydrated catalyst (after Fe(III) precipitation, calcination and rehydration). These complexes can be formed in a zeolite with a low Fe loading (Fe/Al 0.12) under rehydration predominantly from two Fe ions present in the same section of the ferrierite channel, i.e. from two Fe(II) cations located after the calcination of the sample in two opposite β or α sites. The presence of isolated Fe(II)/Fe(III) cations in the sample cannot be excluded due to the strong overlap of the spectra of these ions by the adsorption of Fe(III)-oxo complexes. Our Mössbauer spectroscopy results showed [73] that a dehydration (activation) of the Fe-ferrierite sample resulted in the prevailing presence of Fe(II) cations in the zeolite framework. Moreover, our analysis of the perturbations of skeletal vibrations of the ferrierite framework evidences that 85% of Fe(II) cations are located in the β sites after the dehydration (activation) of the ferrierite sample (Section 3.3.).

The total concentration of the β sites with two Al atoms in the ring and capable to accommodate bare Fe(II) cations in our ferrierite sample was estimated elsewhere [29,72] using Co(II) ions as a probe, for detail see Refs. [74,75]. According to these references, the concentration of Co(II) ions in the β site is Co/Al 0.22, while the maximum loading of bare Co(II) ions is Co/Al 0.31. Thus, 44% of all framework Al atoms are located as pairs in the six-membered ring of the β site.

The Si/Al ratio of the ferrierite sample is 8.6 meaning that there are in average 3.75 Al atoms per unit cell. The Fe exchange at Fe/Al 0.12 corresponds to 0.45 Fe atoms per unit cell ($3.75 * 0.12$). Our FTIR experiments (Fig. 3) reveal that 85% of Fe(II) cations is located in the β sites. Therefore, 0.38 Fe(II) cations per unit cell ($0.45 * 0.85$) are located in the β site. This means that more than every third unit cell contains two Al atoms in the β site balancing Fe(II). There is one six-membered ring per unit cell, which can form a β site if occupied by two Al atoms. A random occupation of the cationic sites by Fe(II) in the zeolite framework then causes that almost every third unit cell ($2 * 0.38 ** 2 = 0.29$) corresponds to a pair of unit cells occupied by two Fe(II) ions located in two neighboring opposite β sites. This Fe occupation agrees well with the observation that binuclear Fe(III) species are significantly present in the hydrated Fe-ferrierite sample. This significant presence of the binuclear Fe(III) species indicates that the distribution of Fe ions in the zeolite channel is not random. Thus, the fraction of Fe accommodated in two adjacent collaborating β sites might be even significantly higher.

This arrangement of two cooperating Fe(II) cations is quite unique and exists only in the ferrierite sample used because of two reasons: the distribution of Al atoms in the ferrierite framework as well as the optimal structural arrangement of the β sites in the ferrierite framework.

8.2. Effect of the Al distribution and framework topology on the formation of isolated and cooperating cationic sites

The difference between the local geometry of the α and β sites is significantly more pronounced than the deviations of the same cationic sites in different zeolite frameworks (ferrierite, the beta zeolite, and ZSM-5) [38,40,41]. This indicates that the small changes of the local geometry of the Fe(II) sites are not responsible for the dramatic differences in the catalytic activity of Fe-ferrierite, Fe-beta, and Fe-ZSM-5.

Different framework topologies can significantly affect the accessibility of Fe(II) ions located in the individual sites of the investigated zeolites. Fe(II) in the α site of the beta zeolite is inaccessible (see Section 4.1). Moreover, different zeolite framework topologies result in different distances of the two Fe(II) cations accommodated in two adjacent collaborating α or β sites in ferrierite, the beta zeolite, and ZSM-5. A comparison of the local structures of the [Fe···NNO Fe] complex present in two cooperating β sites of ferrierite (Fig. 12) and especially the subsequent transition state (Fig. 13) with the arrangements of the α cationic sites in ferrierite, the α and β sites in ZSM-5, and the β sites in the beta zeolite reveals that (1) the α sites in ferrierite and the β sites in ZSM-5 are too close (less than 6.6 Å; see Section 8.1 and Figs. S1 and S3 of the Supplementary material) to accommodate the transition state (2) two α sites in ZSM-5 do not face each other but they are in an acceptable distance and could possibly contain the transition state (Fig. S2 of the Supplementary material); (3) two β sites in the beta zeolite exhibit a proper arrangement similar to that of the two β sites in ferrierite with a slightly longer distance (Fig. S4 of the Supplementary material). Thus, they are also appropriate to form the transition state.

Another important parameter besides the arrangements of the cationic sites that controls the zeolite activity in the N_2O decomposition is the distribution of Al in distinguishable T sites of the zeolite framework as well as the concentration of Al in these T sites. A formation of the [Fe···NNO Fe] complex in two adjacent collaborating α sites in ZSM-5 or β sites in the beta zeolite can occur only when two cooperating sites contain two Al atoms each.

The upper limit of the probability of a formation of adjacent collaborating cationic sites can be estimated from the analysis of the concentration of the α or β sites obtained using bare Co(II) ions as a probe monitored by UV–vis spectroscopy [74,75].

For the investigated ZSM-5 sample, the maximum Co/Al ratio is 0.4 and thus 80% of the framework Al atoms are located in the six-membered rings with two Al atoms. 30% of them correspond to the α site [74]. That means 24% of the framework Al represent the maximum concentration of Al atoms in the six-membered rings forming the α site for this sample. There are 96 T atoms and four rings with the geometry of the α site in a unit cell of ZSM-5. The Si/Al ratio of 13.4 of the ZSM-5 sample used corresponds in average to 6.7 Al atoms per unit cell of which 1.6 Al atoms create the α site ($6.7 * 0.8 * 0.3$). Thus, 1 α site with two Al atoms capable of accommodating Fe(II) corresponds to four other structures with the geometry of the α site but with one or no Al atom. Therefore, the probability of the presence of the α site with two Al atoms is 0.2. Thus, the probability of two adjacent α sites accommodating two Fe(II) cations (the highest occupancy of the α site by Fe(II)) is 0.04 ($0.2 * 0.2$). It should be noted that the low probability (0.04) is not in contradiction with the presence of binuclear Fe complexes in hydrated Fe-exchanged ZSM-5 evidenced by UV–vis spectroscopy. These binuclear complexes can be formed in the hydrated zeolite from Fe ions located in the β sites which concentration is more than twice higher than that of the α sites.

For the beta zeolite sample used, the Si/Al ratio is 15.5 (four Al per unit cell in average), and the maximum Co/Al is 0.45 [41] (90% of the framework Al atoms are located in the six-membered rings with two Al atoms). Fifty-five percent of Co(II) cations are in the β sites [41]. Thus, in average there are 2 ($4 * 0.9 * 0.55$) Al atoms forming a β site in a unit cell. Since there are eight rings with the geometry of the β site in a unit cell and only one of them (1/8) has two Al atoms, the probability of two opposite β sites with Fe(II) in the cationic sites (the highest occupancy of the β site by Fe(II)) is 0.02 ($1/8 * 1/8$). The low probability of the formation of two adjacent β sites with two Al atoms is in good agreement with the UV–vis–NIR spectrum of the hydrated Fe-beta.

The evaluation of the accessibility of cationic sites, distance between adjacent sites, and the probability of the existence of two cooperating sites, each with two Al atoms indicates that the ferrierite structure possesses (1) an appropriate distance between two adjacent β sites, (2) a high probability of a formation of two neighboring β sites each having two Al atoms as well as (3) a linear arrangement of the [Fe···NNO Fe] complex.

The arrangement of two cooperating β sites in the beta zeolite also allows a collaboration of two Fe(II) cations located in these two sites and thus the [Fe···NNO Fe] complex can be formed. The distance between the two Fe(II) cations is however somewhat larger than that in the case of two adjacent β sites in ferrierite. However, the probability of a formation of the [Fe···NNO Fe] complex is low due to the low probability of a formation of two adjacent β sites each having two Al atoms.

On the other hand, the likelihood of the existence of two neighboring cationic sites each having two Al atoms in ZSM-5 is higher than in the beta zeolite but the geometric arrangement of the α sites in the zeolite framework is not suitable for a facile formation of the linear [Fe···NNO Fe] complex. Therefore, Fe-ferrierite exhibits a superior activity in the N_2O decomposition with respect to the other two zeolites used. The activity of Fe-beta and Fe-ZSM-5 is estimated to be significantly weaker and negligible, respectively. This conclusion is in good agreement with the observed activity of the catalysts for the very first steps of the N_2O decomposition, see Section 3.4.).

9. Conclusions

We provided evidence based on our multiple spectroscopy results, DFT calculations, and structural models that two Fe(II) cations coordinated in two adjacent β sites of Fe-ferrierite most likely form the active site responsible for the superior activity of this catalyst in the N_2O decomposition in the low temperature region. This conclusion does not imply that this double iron site which is specific for ferrierite of the optimal Si/Al ratio is the only possible type of active site for the N_2O decomposition. Other types of iron containing species can be responsible for the catalytic activity namely in the high temperature region as well as in the presence of NO.

The calculated Fe–Fe distance of the active site is 7.4 Å. The formation of the active sites results from a combination of (1) a suitable topology of the ferrierite framework and (2) an appropriate distribution of Al in the distinguishable T sites of the ferrierite framework as well as concentration of Al in these T sites. Both six-membered rings forming the two neighboring β sites must contain two Al atoms each (four Al atoms in total).

Two adjacent β sites of Fe-beta can also form an active site with two collaborating Fe(II) cations. However, there are significant differences with respect to ferrierite. The Fe–Fe distance is somewhat longer and, more importantly, the distribution and concentration of Al in the rings with the geometry of the β site lead to a very low probability of occurrence of the active sites with two cooperating Fe(II) cations. This is responsible for the superior activity of Fe-ferrierite relative to Fe-beta.

Two close α sites of the Fe(II) exchanged ZSM-5 zeolite coordinating two collaborating Fe(II) cations can compose the active site. However, the geometrical arrangement of two adjacent α sites is very distant from that of two adjacent β sites in ferrierite. Also the probability of a formation of these active sites is low due to an unfavorable Al distribution and Al concentration in the rings forming the α sites.

The results of our experimental and theoretical investigation show that the order of the activity of the Fe(II) exchanged zeolites is as follows: Fe-ferrierite $\gg$ Fe-beta > Fe-ZSM-5.

Our DFT calculations showed that the accommodation of divalent cation in rings forming cationic sites can lead to a significant rearrangement of the local structure of the zeolite framework. This is in agreement with the results of previous studies indicating that the cations prefer to bind to oxygen atoms of AlO_4 tetrahedra and thus change the structure of the cationic site.

Acknowledgments

This work was financially supported by the Grant Agency of the Academy of Sciences of the Czech Republic (Projects Nos. IAA400400812, IAA400400908, and IAA400400904), the Grant Agency of the Czech Republic (Project No. 203/09/1627), the Academy of Sciences of the Czech Republic (Project No. KAN100400702), and Center of Excellence IDECAT NMP3-CT-2005-011,730. We would like to thank Dr. Kamil Jisa for helpful discussions regarding IR spectroscopy of transition metal exchanged zeolites.

Appendix A. Supplementary material

Supplementary data associated with this article can be found, in the online version, at doi:10.1016/j.jcat.2010.04.008.

References

[1] G.I. Panov, V.I. Sobolev, A.S. Kharitonov, J. Mol. Catal. 61 (1990) 85.
[2] V.N. Parmon, G.I. Panov, A. Uriarte, A.S. Noskov, Catal. Today 100 (2005) 115.
[3] G.D. Pirngruber, P.K. Roy, R. Prins, J. Catal. 246 (2007) 147.
[4] P.K. Roy, R. Prins, G.D. Pirngruber, Appl. Catal. B Environ. 80 (2008) 226.
[5] Z. Sobalik, Transworld Research Network, Zeolites: From Model Materials to Industrial Catalysts 37/661 (2008) 333.
[6] J. Perez-Ramirez, J. Catal. 227 (2004) 512.
[7] E.V. Kondratenko, J. Perez-Ramirez, J. Phys. Chem. B 110 (2006) 22586.
[8] L.V. Pirutko, V.S. Chernyavsky, E.V. Starokon, A.A. Ivanov, A.S. Kharitonov, G.I. Panov, Appl. Catal. B Environ. 91 (2009) 174.
[9] N. Hansen, A. Heyden, A.T. Bell, F.J. Keil, J. Catal. 248 (2007) 213.
[10] N. Hansen, A. Heyden, A.T. Bell, F.J. Keil, J. Phys. Chem. C 111 (2007) 2092.
[11] A. Heyden, A.T. Bell, F.J. Keil, J. Catal. 233 (2005) 26.
[12] A. Heyden, N. Hansen, A.T. Bell, F.J. Keil, J. Phys. Chem. B 110 (2006) 17096.
[13] A. Heyden, B. Peters, A.T. Bell, F.J. Keil, J. Phys. Chem. B 109 (2005) 1857.
[14] B.R. Wood, J.A. Reimer, A.T. Bell, J. Catal. 209 (2002) 151.
[15] M.F. Fellah, I. Onal, Catal. Today 137 (2008) 410.
[16] I. Melian-Cabrera, C. Mentruit, J.A.Z. Pieterse, R.W. van den Brink, G. Mul, F. Kapteijn, J.A. Moulijn, Catal. Commun. 6 (2005) 301.
[17] A.H. Oygarden, J. Perez-Ramirez, Appl. Catal. B Environ. 65 (2006) 163.
[18] J. Perez-Ramirez, J.C. Groen, A. Bruckner, M.S. Kumar, U. Bentrup, M.N. Debbagh, L.A. Villaescusa, J. Catal. 232 (2005) 318.
[19] J.A.Z. Pieterse, G.D. Pirngruber, J.A. van Bokhoven, S. Booneveld, Appl. Catal. B Environ. 71 (2007) 16.
[20] M. Mauvezin, G. Delahay, B. Coq, S. Kieger, J.C. Jumas, J. Olivier-Fourcade, J. Phys. Chem. B 105 (2001) 928.
[21] K. Jisa, J. Novakova, M. Schwarze, A. Vondrova, S. Sklenak, Z. Sobalik, J. Catal. 262 (2009) 27.
[22] W.B. Tolman, Angew. Chem., Int. Ed. 49 (2010) 1018.
[23] H. Guesmi, D. Berthomieu, B. Bromley, B. Coq, L. Kiwi-Minsker, Phys. Chem. Chem. Phys. 12 (2010) 2873.
[24] H. Guesmi, D. Berthomieu, L. Kiwi-Minsker, J. Phys. Chem. C 112 (2008) 20319.
[25] M. Rivallan, G. Ricchiardi, S. Bordiga, A. Zecchina, J. Catal. 264 (2009) 104.
[26] Q. Shen, L.D. Li, Z.P. Hao, Z.P. Xu, Appl. Catal. B Environ. 84 (2008) 734.
[27] CZ 293917 B6 (2001).
[28] L. Capek, V. Kreibich, J. Dedecek, T. Grygar, B. Wichterlova, Z. Sobalik, J.A. Martens, R. Brosius, V. Tokarova, Microporous Mesoporous Mater. 80 (2005) 279.
[29] Z. Sobalik, J. Dedecek, D. Kaucky, B. Wichterlova, L. Drozdova, R. Prins, J. Catal. 194 (2000) 330.
[30] Z. Sobalik, Z. Tvaruzkova, B. Wichterlova, Microporous Mesoporous Mater. 25 (1998) 225.
[31] P. Sarv, B. Wichterlova, J. Cejka, J. Phys. Chem. B 102 (1998) 1372.
[32] J.M. Thomas, J. Klinowski, Adv. Catal. 33 (1985) 199.
[33] C.A. Fyfe, G.C. Gobbi, G.J. Kennedy, J. Phys. Chem. 88 (1984) 3248.
[34] G. Engelhardt, U. Lohse, E. Lippmaa, M. Tarmak, M. Magi, Z. Anorg. Allg. Chem. 482 (1981) 49.
[35] L. Lopes, J. de Laat, B. Legube, Inorg. Chem. 41 (2002) 2505.
[36] A.C. Scheinost, A. Chavernas, V. Barron, J. Torrent, Clay Clay Miner. 46 (1998) 528.
[37] B. Wichtelova, Z. Sobalik, J. Dedecek, Appl. Catal. B Environ. 41 (2003) 97.
[38] J. Dedecek, D. Kaucky, B. Wichterlova, Microporous Mesoporous Mater. 35–36 (2000) 483.
[39] J. Dedecek, B. Wichterlova, J. Phys. Chem. B 103 (1999) 1462.
[40] D. Kaucky, J. Dedecek, B. Wichterlova, Microporous Mesoporous Mater. 31 (1999) 75.
[41] J. Dedecek, L. Capek, D. Kaucky, Z. Sobalik, B. Wichterlova, J. Catal. 211 (2002) 198.
[42] W.J. Mortier, J. Phys. Chem. 81 (1977) 1334.
[43] J.L. Schlenker, J.J. Pluth, J.V. Smith, Mater. Res. Bull. 13 (1978) 169.
[44] M.C. Dalconi, A. Alberti, G. Cruciani, J. Phys. Chem. B 107 (2003) 12973.

[45] M.C. Dalconi, A. Alberti, G. Cruciani, P. Ciambelli, E. Fonda, Microporous Mesoporous Mater. 62 (2003) 191.
[46] M.C. Dalconi, G. Cruciani, A. Alberti, P. Ciambelli, M.T. Rapacciuolo, Microporous Mesoporous Mater. 39 (2000) 423.
[47] D. Berthomieu, N. Jardillier, G. Delahay, B. Coq, A. Goursot, Catal. Today 110 (2005) 294.
[48] M.H. Groothaert, K. Pierloot, A. Delabie, R.A. Schoonheydt, Phys. Chem. Chem. Phys. 5 (2003) 2135.
[49] S.A. McMillan, R.Q. Snurr, L.J. Broadbelt, Microporous Mesoporous Mater. 68 (2004) 45.
[50] L. Benco, T. Bucko, R. Grybos, J. Hafner, Z. Sobalik, J. Dedecek, J. Hrusak, J. Phys. Chem. C 111 (2007) 586.
[51] G. Vezzalini, S. Quartieri, E. Galli, A. Alberti, G. Cruciani, A. Kvick, Zeolites 19 (1997) 323.
[52] J.M. Newsam, M.M.J. Treacy, W.T. Koetsier, C.B. Degruyter, Proc. Roy. Soc. Lond. A Math. 420 (1988) 375.
[53] I.J. Pickering, P.J. Maddox, J.M. Thomas, A.K. Cheetham, J. Catal. 119 (1989) 261.
[54] G. Kresse, J. Furthmuller, Phys. Rev. B 54 (1996) 11169.
[55] G. Kresse, J. Furthmuller, Comput. Mater. Sci. 6 (1996) 15.
[56] G. Kresse, J. Hafner, Phys. Rev. B 48 (1993) 13115.
[57] G. Kresse, J. Hafner, Phys. Rev. B 49 (1994) 14251.
[58] L. Benco, T. Bucko, R. Grybos, J. Hafner, Z. Sobalik, J. Dedecek, S. Sklenak, J. Hrusak, J. Phys. Chem. C 111 (2007) 9393.
[59] P.E. Blochl, Phys. Rev. B 50 (1994) 17953.
[60] G. Kresse, D. Joubert, Phys. Rev. B 59 (1999) 1758.
[61] J.P. Perdew, J.A. Chevary, S.H. Vosko, K.A. Jackson, M.R. Pederson, D.J. Singh, C. Fiolhais, Phys. Rev. B 46 (1992) 6671.
[62] J.P. Perdew, Y. Wang, Phys. Rev. B 45 (1992) 13244.
[63] G. Henkelman, H. Jonsson, J. Chem. Phys. 111 (1999) 7010.
[64] A. Heyden, A.T. Bell, F.J. Keil, J. Chem. Phys. 123 (2005) 224101.
[65] S. Nose, J. Chem. Phys. 81 (1984) 511.
[66] L. Verlet, Phys. Rev. 159 (1967) 98.
[67] L. Verlet, Phys. Rev. 165 (1968) 201.
[68] M.P. Attfield, S.J. Weigel, A.K. Cheetham, J. Catal. 170 (1997) 227.
[69] W.J. Mortier, J.J. Pluth, J.V. Smith, Mater. Res. Bull. 10 (1975) 1037.
[70] M.C. Dalconi, G. Cruciani, A. Alberti, P. Ciambelli, Catal. Today (2005) 345.
[71] M.P. Attfield, S.J. Weigel, A.K. Cheetham, J. Catal. 172 (1997) 274.
[72] L. Drozdova, R. Prins, J. Dedecek, Z. Sobalik, B. Wichterlova, J. Phys. Chem. B 106 (2002) 2240.
[73] M. Schwarze, Z. Sobalik, E.G. Caspary, D. Niznansky, Czech. J. Phys. 56 (2006) E147.
[74] J. Dedecek, D. Kaucky, B. Wichterlova, O. Gonsiorova, Phys. Chem. Chem. Phys. 4 (2002) 5406.
[75] J. Dedecek, D. Kaucky, B. Wichterlova, Chem. Commun. (2001) 970.